Investigating a Mn:Ni:Ce Metallic Nanocomposite-Enhanced Bulk Heterojunction Inverted Organic Solar Cell Device

By

K.P.A Sikosana

Submitted in partial fulfilment for the degree:
BSc Physics Honours

University of Pretoria
Department of Physics
Supervisor: Prof M.M. Diale
Co-supervisors: T.E. Seimela, Dr M.S.G Hamed

October 2025

Abstract

This study investigates the incorporation of Mn:Ni:Ce trimetallic nanoparticles into the bulk heterojunction active layer of inverted organic solar cells based on a PCBM:PCDTBT blend. The nanoparticles were synthesised via a wet chemical process and characterised using SEM and EDS, revealing predominantly spherical particles with a strong cerium dominance, indicating incomplete trimetallic alloy formation. Devices fabricated with varying nanoparticle concentrations were evaluated using J-V measurements, quantum efficiency, UV-Vis absorption, and impedance spectroscopy. The optimal nanoparticle loading of 1 mg led to a power conversion efficiency of 6.63%, nearly tripling that of the pristine device, through enhanced fill factor, short-circuit current, and open-circuit voltage. Optical measurements showed broader spectral absorption and increased photon harvesting attributed to localised surface plasmon resonance effects. Impedance analysis confirmed improved and more uniform charge transport at optimal loading, while higher concentrations caused aggregation and recombination losses. These findings demonstrate that controlled nanoparticle integration enhances organic solar cell performance, with further research needed to optimise nanoparticle composition and stability.

Table of Contents

List of Figures

List of Tables

Chapter 1

Introduction

1.1. Background and motivation: A South African Backdrop

South Africa's energy mix remains heavily reliant on fossil fuels, with a 2023 Energy Commission report indicating that carbon-based sources account for approximately 85% of total energy production [1]. At a time when much of the global community is accelerating the transition toward renewable energy, South Africa stands at a critical crossroads in shaping its energy future. Decarbonisation, the reduction or elimination of anthropogenic carbon emissions, has become an urgent priority. As a signatory to the Paris Climate Agreement, South Africa has committed to achieving net zero emissions by the second half of the century [2]. Meeting this target will require phasing out coal, oil, and natural gas in favour of cleaner energy sources such as wind, solar, biofuels, solar thermal, nuclear, and hydroelectric power [3-5].

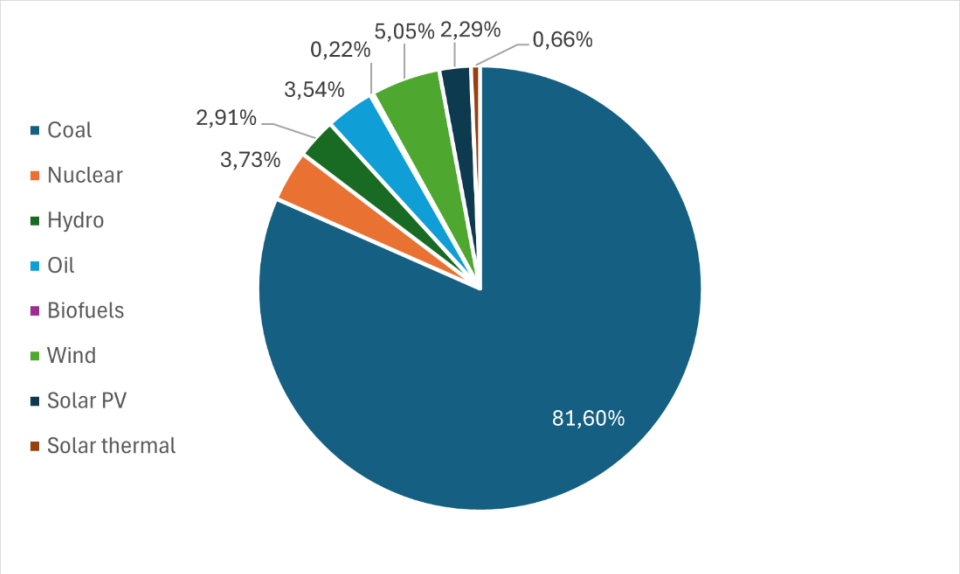

Figure 1: Energy Mix in South Africa [1]

South Africa is marked by deep socio-economic inequality, compounded by a persistently high unemployment rate [6]. In the first quarter of 2015, the official unemployment rate among youth

aged 15 to 34 stood at 36.9%. By the first quarter of 2025, this figure had risen to 46.1%, reflecting a 9.2 percentage point increase and underscoring the worsening employment prospects for millions of young people [7]. Within this challenging context, the rising cost of electricity places an additional burden on households and businesses. The National Energy Regulator of South Africa (NERSA) has approved a 12.74% tariff increase for the 2025/26 financial year [8], intensifying the strain of already elevated energy prices.

Under these conditions, exploring avenues for self-generation of electricity becomes not only practical but also necessary. With approximately 2,500 hours of sunshine annually [9-11], South Africa ranks among the sunniest regions in the world, making solar power a particularly attractive option. However, conventional photovoltaic technologies rely largely on crystalline silicon [12, 13], which is costly to source and manufacture [14], while installation expenses remain high [15, 16]. This raises a critical question: are there more cost-effective solar technologies?

Beyond traditional silicon photovoltaics, alternative approaches such as amorphous silicon, perovskite, tandem, dye-sensitised, and polymer-based solar cells have emerged. Among these, polymer (organic) solar cells represent a promising pathway toward affordable, scalable, and sustainable solar energy production [17]. Nevertheless, their practical adoption remains limited, and significant research is still required to improve efficiency, stability, and manufacturability [14, 18-24]. Institutions such as the National Renewable Energy Laboratory (NREL) continuously track and benchmark progress in photovoltaic technologies, providing updated records of state-of-the-art efficiencies and highlighting research trends that guide the broader solar cell community as shown in figure 2 below [25].

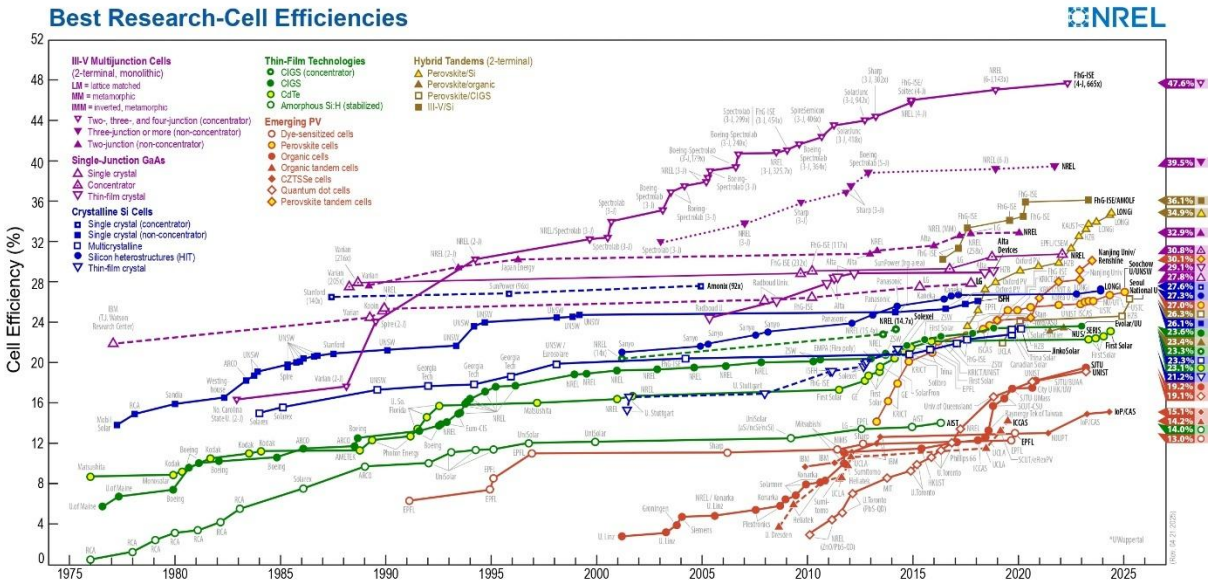

Figure 2: Timeline of best efficiencies of solar cell (NREL)

1.2. Organic Solar Cell Theory

Organic Solar Cells (OSC) are a class of semiconductor devices in which the conventional p–n junction is replaced with organic compounds that possess semiconducting and conductive properties [22, 23, 26, 27]. The principal advantage of these materials lies in their affordability, as they are generally less expensive to produce and process compared to their silicon-based counterparts [17]. Moreover, their compatibility with low-cost fabrication techniques, such as solution processing and roll-to-roll printing, positions them as a promising alternative for large-scale, cost-effective solar energy generation [21].

1.2.1 Architecture

OSC research has advanced significantly over the past few decades, with one major milestone being the transition from bilayer to bulk heterojunction (BHJ) structures. The BHJ architecture enables more efficient charge separation and transport by blending donor and acceptor materials within the active layer, thereby overcoming limitations of earlier bilayer designs [28]. Within the BHJ framework, two main device configurations are commonly employed: conventional and inverted [18]. In the conventional structure, the typical sequence is Glass/ITO/Electron Transport Layer/Active Layer/Hole Transport Layer/Cathode. By contrast,

the inverted structure follows Glass/ITO/Hole Transport Layer/Active Layer/Electron Transport Layer/Anode. The key distinction lies in the role of the transparent ITO-coated glass substrate, which functions as the cathode in the conventional design and as the anode in the inverted design. The overall device can be visualised as a layered stack, like a sandwich, where each layer serves a specific function in enabling light absorption, charge transport, and current collection [29-31].

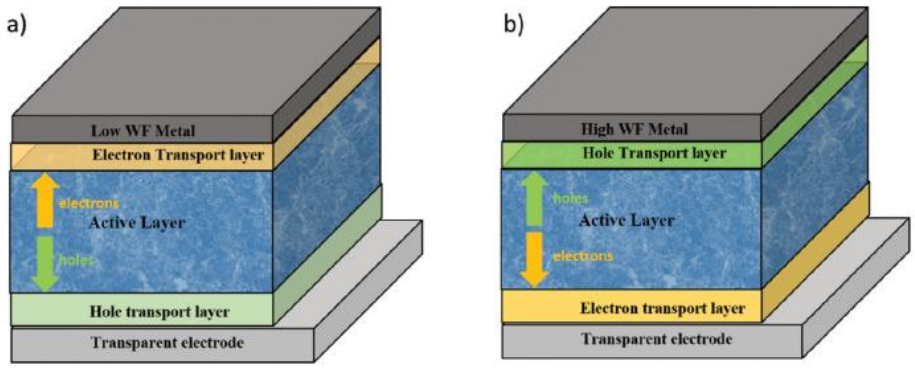

Figure 3: a) Conventional vs b) Inverted OSC device architectures [18]

Indium Tin Oxide (ITO) is the most widely employed transparent electrode in photovoltaic devices due to its excellent electrical conductivity, high optical transmittance, and suitable work function. Initially developed for inorganic solar cells, ITO was rapidly incorporated into organic devices because of these advantageous properties [32]. A key benefit is its high transmittance, exceeding 80% across the visible region of the solar spectrum, which enables efficient illumination from the ITO side of the device.

Dependent on whether one employs a conventional or inverted device structure, the choice of high or low work function metals for the electrodes becomes critical [33]. High work function materials are typically used as anodes to facilitate hole extraction, while low work function metals serve as cathodes for electron collection. However, low work function metals are highly susceptible to oxidation, which undermines interfacial stability and accelerates device degradation [34, 35]. A widely adopted strategy to address this limitation is the inverted configuration [29, 36], in which ITO functions as the cathode and a high work function metal is

used as the anode. Because pure ITO is not inherently suitable for efficient electron extraction, it is commonly modified with interfacial layers that adjust its effective work function. Typical electron-transporting interlayers include metal oxides such as Zinc Oxide (ZnO), which enhance electron collection while suppressing recombination losses [37]. On the anode side, Molybdenum Trioxide (MoO_3) has emerged as a particularly effective interlayer material. Its high work function promotes efficient hole extraction, while simultaneously blocking electrons from reaching the electrode. In addition, MoO_3 provides excellent chemical stability and smoothens interfacial energy level alignment, thereby reducing contact resistance and improving device durability [20, 38, 39].

1.2.2 Active layer

The photoactive layer of BHJ OSCs is the most critical component, characterised by a nanoscale bi-continuous morphology comprising intermixed donor and acceptor phases [18, 40]. This photoactive layer is responsible for converting absorbed photons, within its optical absorption range, into charge carriers [21, 23, 26, 27, 41]. A wide variety of material systems have been explored for BHJ photoactive layers, including polymer-fullerene blends, polymer-small molecule systems, all-polymer blends, all-small molecule systems, and even multi-component OSCs [42]. To optimise charge generation and transport, the crystallinity and phase separation of BHJ blends can be tuned through several post-treatment strategies such as Thermal Annealing, Solvent Vapour Annealing or in the incorporation of Solid Additives [43], an idea which will be important when metallic nanoparticles are discussed.

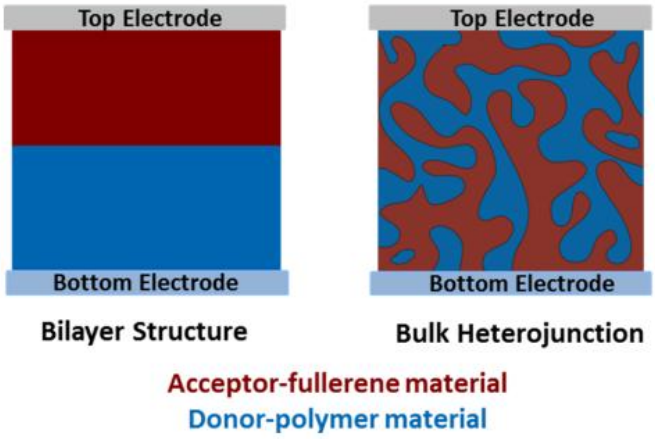

Figure 4: The difference between bilayer and bulk heterojunction solar cells [44]

Despite significant progress, the performance of OSCs remains limited by their inherently thin active layers, which restrict the fraction of sunlight absorbed. Since increasing thickness often compromises charge extraction due to the short exciton diffusion length [45], strategies to enhance light absorption without sacrificing transport have been widely explored.

One promising avenue is the integration of metallic nanoparticles (NPs) into the device [46, 47]. These NPs can support localised surface plasmon resonances (LSPRs), which amplify the local electromagnetic field and increase optical scattering within the active layer, thereby boosting photon harvesting [48]. However, while some studies have investigated mono- and bimetallic nanoparticles in polymer blends [49], reports on trimetallic nanocomposite systems are scarce, especially in inverted architectures. Furthermore, the impact of embedding such NPs directly into a PCBM:PCDTBT blend on optical, morphological, and electrical properties remains unprobed.

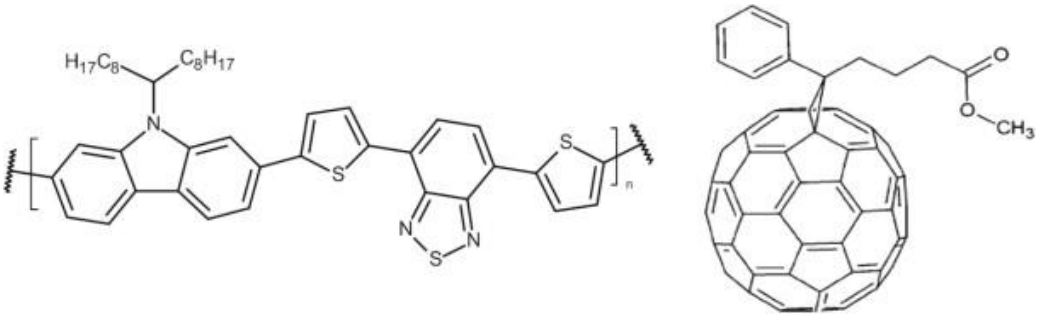

Figure 5: PCDTBT (left) and PCBM (right) [50]

1.3 Aims and objectives

The overarching aim of this research is to investigate the influence of Mn:Ni:Ce trimetallic nanoparticles on the performance of inverted organic solar cells based on a PCBM:PCDTBT active layer.

The specific objectives are to:

1. Provide a concise theoretical overview of organic solar cells, with emphasis on device physics and the role of inverted architectures.
2. Synthesise and characterise Mn:Ni:Ce NPs using SEM and EDS.
3. Fabricate inverted OSC devices with the structure ITO/ZnO/PCBM:PCDTBT/MoO_3/Ag, both with and without embedded NPs.
4. Evaluate the effect of nanoparticle incorporation on device properties using PCE, UV-Vis spectroscopy, Quantum efficiency, and impedance spectroscopy.
5. Compare the obtained results with literature reports on mono- and bimetallic nanoparticle incorporation in OSCs, to assess the novelty and effectiveness of the trimetallic nanocomposite approach.

1.4. Structure of the research paper

Chapter 1: Background and motivation

Chapter 2: Nanoparticles

Chapter 3: Experimental Method

Chapter 4: Results and Discussion

Chapter 5: Conclusion

1.5. References

[1] IEA. "IEA Electricity Information." https://www.iea.org/data-and-statistics/data-product/electricity-information (accessed 18 July, 2025).

[2] A. Modise, "Minister Edna Molewa signs Paris Agreement on climate change," ed: Department of Forestry, Fisheries and Environment, 2016.

[3] R.-H. Hechelmann, A. Paris, N. Buchenau, and F. Ebersold, "Decarbonisation strategies for manufacturing: A technical and economic comparison," *Renewable and Sustainable Energy Reviews,* vol. 188, p. 113797, 2023/12/01/ 2023, doi: https://doi.org/10.1016/j.rser.2023.113797.

[4] E. Tvinnereim and M. Mehling, "Carbon pricing and deep decarbonisation," *Energy Policy,* vol. 121, pp. 185–189, 2018/10/01/ 2018, doi: https://doi.org/10.1016/j.enpol.2018.06.020.

[5] I. Rattle, A. Gailani, and P. G. Taylor, "Decarbonisation strategies in industry: going beyond clusters," *Sustainability Science,* vol. 19, no. 1, pp. 105–123, 2024/01/01 2024, doi: 10.1007/s11625-023-01313-4.

[6] C. W. Kabudula, B. Houle, M. A. Collinson, K. Kahn, S. Tollman, and S. Clark, "Assessing Changes in Household Socioeconomic Status in Rural South Africa, 2001–2013: A

Distributional Analysis Using Household Asset Indicators," *Social Indicators Research,* vol. 133, no. 3, pp. 1047–1073, 2017/09/01 2017, doi: 10.1007/s11205-016-1397-z.

[7] S. S. Africa. "South Africa's Youth in the Labour Market: A Decade in Review." Department of Statistics South Africa. https://www.statssa.gov.za/?p=18398 (accessed 18 June, 2025).

[8] ESKOM, "Tariffs and Charges Booklet 2025 - 2026." [Online]. Available: https://www.eskom.co.za/distribution/wp-content/uploads/2025/07/Tariff-booklet2.pdf

[9] I. M. Smarte Anekwe, S. O. Akpasi, M. M. Mkhize, H. Zhou, R. T. Moyo, and L. Gaza, "Renewable energy investments in South Africa: Potentials and challenges for a sustainable transition - a review," (in eng), *Sci Prog,* vol. 107, no. 2, p. 368504241237347, Apr–Jun 2024, doi: 10.1177/00368504241237347.

[10] N. Xaba, "Whose just energy transition? A South African perspective," *WIREs Energy and Environment,* vol. 12, no. 5, p. e478, 2023, doi: https://doi.org/10.1002/wene.478.

[11] D. o. M. Resources. "Solar Power." https://www.dmre.gov.za/energy-resources/energy-sources/renewable-alternative-fuels/solar-power (accessed 19 July, 2025).

[12] L. Hernández-Callejo, S. Gallardo-Saavedra, and V. Alonso-Gómez, "A review of photovoltaic systems: Design, operation and maintenance," *Solar Energy,* vol. 188, pp. 426–440, 2019/08/01/ 2019, doi: https://doi.org/10.1016/j.solener.2019.06.017.

[13] M. Jacoby, "The future of low-cost solar cells," *Chem. Eng. News,* vol. 94, no. 18, pp. 30–35, 2016.

[14] Y.-J. Lee, B.-S. Kim, S. M. Ifitiquar, C. Park, and J. Yi, "Silicon solar cells: Past, present and the future," *Journal of the Korean Physical Society,* vol. 65, no. 3, pp. 355–361, 2014/08/01 2014, doi: 10.3938/jkps.65.355.

[15] M. Sodhi, L. Banaszek, C. Magee, and M. Rivero-Hudec, "Economic Lifetimes of Solar Panels," *Procedia CIRP,* vol. 105, pp. 782–787, 2022/01/01/ 2022, doi: https://doi.org/10.1016/j.procir.2022.02.130.

[16] H. Terzioglu, F. A. Kazan, and M. Arslan, "A New Approach to the Installation of Solar Panels," in *2015 2nd International Conference on Information Science and Control Engineering*, 24–26 April 2015 2015, pp. 573–577, doi: 10.1109/ICISCE.2015.133.

[17] J. Dhilipan, N. Vijayalakshmi, D. B. Shanmugam, R. Jai Ganesh, S. Kodeeswaran, and S. Muralidharan, "Performance and efficiency of different types of solar cell material – A review," *Materials Today: Proceedings,* vol. 66, pp. 1295–1302, 2022/01/01/ 2022, doi: https://doi.org/10.1016/j.matpr.2022.05.132.

[18] L. Duan and A. Uddin, "Progress in Stability of Organic Solar Cells," *Advanced Science,* vol. 7, no. 11, p. 1903259, 2020, doi: https://doi.org/10.1002/advs.201903259.

[19] D. Luo, W. Jang, D. D. Babu, M. S. Kim, D. H. Wang, and A. K. K. Kyaw, "Recent progress in organic solar cells based on non-fullerene acceptors: materials to devices," *Journal of Materials Chemistry A,* vol. 10, no. 7, pp. 3255–3295, 2022.

[20] D. W. Zhao *et al.*, "Optimization of an inverted organic solar cell," *Solar Energy Materials and Solar Cells,* vol. 94, no. 6, pp. 985–991, 2010, doi: 10.1016/j.solmat.2010.02.010.

[21] N. Yeh and P. Yeh, "Organic solar cells: Their developments and potentials," *Renewable and Sustainable Energy Reviews,* vol. 21, pp. 421–431, 2013/05/01/ 2013, doi: https://doi.org/10.1016/j.rser.2012.12.046.

[22] D. Wöhrle and D. Meissner, "Organic Solar Cells," *Advanced Materials,* vol. 3, no. 3, pp. 129–138, 1991, doi: 10.1002/adma.19910030303.

[23] H. Spanggaard and F. C. Krebs, "A brief history of the development of organic and polymeric photovoltaics," *Solar Energy Materials and Solar Cells,* vol. 83, no. 2, pp. 125–146, 2004, doi: 10.1016/j.solmat.2004.02.021.

[24] J. D. Servaites, M. A. Ratner, and T. J. Marks, "Organic solar cells: A new look at traditional models," *Energy & Environmental Science,* 10.1039/C1EE01663F vol. 4, no. 11, pp. 4410–4422, 2011, doi: 10.1039/C1EE01663F.

[25] N. R. E. Laboratory. "Best Research-Cell Efficiency Chart." US Department of Energy. https://www.nrel.gov/pv/cell-efficiency (accessed 18 July, 2025).

[26] W. Tress, "Organic Solar Cells," in *Organic Solar Cells: Theory, Experiment, and Device Simulation*, W. Tress Ed. Cham: Springer International Publishing, 2014, pp. 67–214.

[27] T. M. Clarke and J. R. Durrant, "Charge Photogeneration in Organic Solar Cells," *Chemical Reviews,* vol. 110, no. 11, pp. 6736–6767, 2010/11/10 2010, doi: 10.1021/cr900271s.

[28] A. J. Heeger, "25th Anniversary Article: Bulk Heterojunction Solar Cells: Understanding the Mechanism of Operation," *Advanced Materials,* vol. 26, no. 1, pp. 10–28, 2014, doi: https://doi.org/10.1002/adma.201304373.

[29] S. K. Hau, H.-L. Yip, and A. K. Y. Jen, "A Review on the Development of the Inverted Polymer Solar Cell Architecture," *Polymer Reviews,* vol. 50, no. 4, pp. 474–510, 2010/10/28 2010, doi: 10.1080/15583724.2010.515764.

[30] H. Mehdizadeh Rad, F. Zhu, and J. Singh, "Profiling exciton generation and recombination in conventional and inverted bulk heterojunction organic solar cells," *Journal of Applied Physics,* vol. 124, no. 8, 2018, doi: 10.1063/1.5031062.

[31] S. Lattante, "Electron and Hole Transport Layers: Their Use in Inverted Bulk Heterojunction Polymer Solar Cells," *Electronics,* vol. 3, no. 1, pp. 132–164, 2014. [Online]. Available: https://www.mdpi.com/2079-9292/3/1/132.

[32] T. Mizrah and D. Adler, "Indium—Tin—Oxide—Silicon heterojunction photovoltaic devices," *IEEE Transactions on Electron Devices,* vol. 24, no. 4, 1977, doi: 10.1109/T-ED.1977.18758.

[33] B. de Boer, A. Hadipour, M. M. Mandoc, T. van Woudenbergh, and P. W. M. Blom, "Tuning of Metal Work Functions with Self-Assembled Monolayers," *Advanced Materials,* vol. 17, no. 5, pp. 621–625, 2005, doi: https://doi.org/10.1002/adma.200401216.

[34] B. Shamieh *et al.*, "Correlating the effective work function at buried organic/metal interfaces with organic solar cell characteristics," *Journal of Materials Chemistry C,* 10.1039/C8TC02381F vol. 6, no. 30, pp. 8060–8068, 2018, doi: 10.1039/C8TC02381F.

[35] H. Ju *et al.*, "Interplay between Interfacial Structures and Device Performance in Organic Solar Cells: A Case Study with the Low Work Function Metal, Calcium," *ACS Applied Materials & Interfaces,* vol. 8, no. 3, pp. 2125–2131, 2016/01/27 2016, doi: 10.1021/acsami.5b10641.

[36] M. Abdallaoui, N. Sengouga, A. Chala, A. F. Meftah, and A. M. Meftah, "Comparative study of conventional and inverted P3HT: PCBM organic solar cell," *Optical Materials,* vol. 105, p. 109916, 2020/07/01/ 2020, doi: https://doi.org/10.1016/j.optmat.2020.109916.

[37] C. Thu *et al.*, "Role of the Metal-Oxide Work Function on Photocurrent Generation in Hybrid Solar Cells," *Scientific Reports,* vol. 8, no. 1, p. 3559, 2018/02/23 2018, doi: 10.1038/s41598-018-21721-2.

[38] C. Girotto, E. Voroshazi, D. Cheyns, P. Heremans, and B. P. Rand, "Solution-Processed MoO3 Thin Films As a Hole-Injection Layer for Organic Solar Cells," *ACS Applied Materials & Interfaces,* vol. 3, no. 9, pp. 3244–3247, 2011/09/28 2011, doi: 10.1021/am200729k.

[39] G. Wang *et al.*, "Preparation and characterization of MoO3 hole-injection layer for organic solar cell fabrication and optimization," *Solar Energy Materials and Solar Cells,* vol. 120, pp. 603–609, 2014/01/01/ 2014, doi: https://doi.org/10.1016/j.solmat.2013.10.002.

[40] F. Etzold *et al.*, "Ultrafast Exciton Dissociation Followed by Nongeminate Charge Recombination in PCDTBT:PCBM Photovoltaic Blends," *Journal of the American Chemical Society,* vol. 133, no. 24, pp. 9469–9479, 2011/06/22 2011, doi: 10.1021/ja201837e.

[41] T. L. Benanti and D. Venkataraman, "Organic Solar Cells: An Overview Focusing on Active Layer Morphology," *Photosynthesis Research,* vol. 87, no. 1, pp. 73–81, 2006/01/01 2006, doi: 10.1007/s11120-005-6397-9.

[42] J. Yi, G. Zhang, H. Yu, and H. Yan, "Advantages, challenges and molecular design of different material types used in organic solar cells," *Nature Reviews Materials,* vol. 9, no. 1, pp. 46–62, 2023, doi: 10.1038/s41578-023-00618-1.

[43] C. Cui and Y. Li, "Morphology optimization of photoactive layers in organic solar cells," *Aggregate,* vol. 2, no. 2, p. e31, 2021, doi: https://doi.org/10.1002/agt2.31.

[44] H.-J. Wang, C.-P. Chen, and R.-J. Jeng, "Polythiophenes Comprising Conjugated Pendants for Polymer Solar Cells: A Review," *Materials,* vol. 7, pp. 2411–2439, 03/27 2014, doi: 10.3390/ma7042411.

[45] A. Armin, A. Yazmaciyan, M. Hambsch, J. Li, P. L. Burn, and P. Meredith, "Electro-Optics of Conventional and Inverted Thick Junction Organic Solar Cells," *ACS Photonics,* vol. 2, no. 12, pp. 1745–1754, 2015/12/16 2015, doi: 10.1021/acsphotonics.5b00441.

[46] M. M. Shahjamali, M. Salvador, M. Bosman, D. S. Ginger, and C. Xue, "Edge-Gold-Coated Silver Nanoprisms: Enhanced Stability and Applications in Organic Photovoltaics and Chemical Sensing," *The Journal of Physical Chemistry C,* vol. 118, no. 23, pp. 12459–12468, 2014/06/12 2014, doi: 10.1021/jp501884s.

[47] M. Salvador *et al.*, "Electron Accumulation on Metal Nanoparticles in Plasmon-Enhanced Organic Solar Cells," *ACS Nano,* vol. 6, no. 11, pp. 10024–10032, 2012/11/27 2012, doi: 10.1021/nn303725v.

[48] S. D. Standridge, G. C. Schatz, and J. T. Hupp, "Distance Dependence of Plasmon-Enhanced Photocurrent in Dye-Sensitized Solar Cells," *Journal of the American Chemical Society,* vol. 131, no. 24, pp. 8407–8409, 2009/06/24 2009, doi: 10.1021/ja9022072.

[49] X. Li, W. C. H. Choy, H. Lu, W. E. I. Sha, and A. H. P. Ho, "Efficiency Enhancement of Organic Solar Cells by Using Shape-Dependent Broadband Plasmonic Absorption in Metallic Nanoparticles," *Advanced Functional Materials,* vol. 23, no. 21, pp. 2728–2735, 2013, doi: https://doi.org/10.1002/adfm.201202476.

[50] T. M. Clarke *et al.*, "Charge carrier mobility, bimolecular recombination and trapping in polycarbazole copolymer:fullerene (PCDTBT:PCBM) bulk heterojunction solar cells," *Organic Electronics,* vol. 13, no. 11, pp. 2639–2646, 2012/11/01/ 2012, doi: https://doi.org/10.1016/j.orgel.2012.07.037.

Chapter 2

Nanoparticles

2.1. Introduction

The prefix “nano” originates from the Greek word for “dwarf” and denotes a scale of 10^{-9}, or one billionth of a metre [1]. Nanoscience is therefore concerned with the study and manipulation of matter at this scale, which is far removed from everyday human perception yet exerts profound influence on many of the macroscopic properties observed in nature and technology. At the nanoscale, materials often exhibit unique optical, electronic, and catalytic behaviours that differ significantly from their bulk counterparts, making them highly relevant to the LSPR phenomenon mentioned in the previous chapter.

Miniaturisation, the trend of designing and producing increasingly smaller mechanical, optical, and electronic devices, also underpins NP synthesis [2]. As a miniaturisation technique, nanoparticle synthesis can be broadly divided into two main approaches: top-down and bottom-up. In the top-down approach, bulk materials are broken down into nanoscale structures, whereas the bottom-up approach builds nanoparticles by assembling them from atomic or molecular constituents [3].

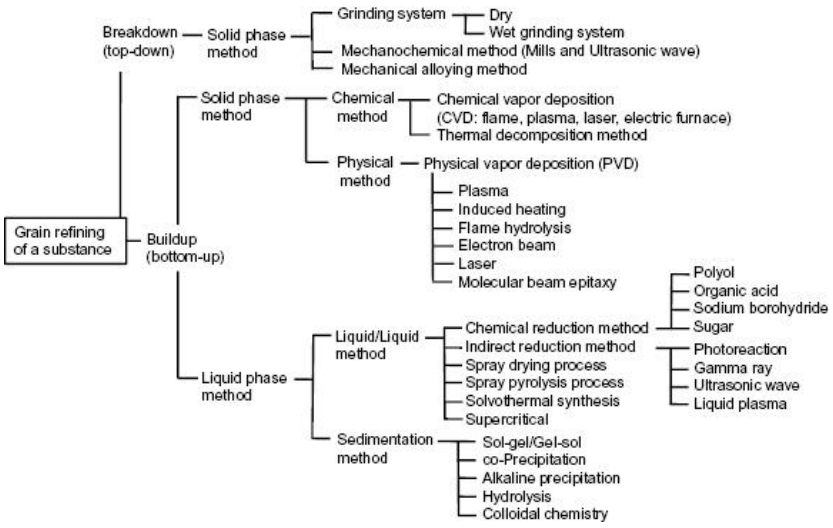

Figure 6: Nanoparticle Synthesis techniques [1]

Effective synthesis of NPs involves precise control over particle size, size distribution, and morphology to ensure uniformity and desired properties. It also requires careful regulation of the crystal structure and composition, along with strict minimisation of impurities to obtain pristine, high-quality samples. Just as important is the ability to reproduce the synthesis consistently and scale it up from laboratory experiments to industrial production, making the process both reliable and practical.

Table 1: Classification and Applications of Nanoparticles [4]

Type of Nanoparticles	Description / Structure	Key Properties	Applications
Carbon-based NPs (Fullerenes & CNTs)	Fullerenes: globular hollow cages of sp^2 carbon units (pentagons & hexagons). CNTs: tubular structures (1–2 nm diameter), single-, double-, or multi-walled.	High strength, conductivity, electron affinity, structural adaptability.	Electronics, materials science, nanomedicine.
Metal NPs	Purely metallic (e.g., Cu, Ag, Au). Exhibit LSPR.	Distinctive electrical & optical properties, tuneable by size, facet, and shape.	Sensing, catalysis, medicine, photonics.
Ceramic NPs	Inorganic, non-metallic; can be amorphous, polycrystalline, dense, porous, or hollow.	Heat resistance, durability, stability.	Coatings, catalysts, batteries.
Lipid-based NPs	Composed of lipid moieties; spherical (10–1,000 nm). Contain a solid lipid core with lipophilic molecules.	Biocompatible, versatile drug carriers.	Drug delivery, nanomedicine, vaccines.
Semiconductor NPs	Between metals and non-metals, absorb & emit light.	Unique electronic & optical properties; tuneable band gaps.	Solar cells, LEDs, transistors, bioimaging, cancer therapy.
Polymeric NPs	Organic polymers, 1–1,000 nm; drugs can be adsorbed on the surface or encapsulated inside.	Biodegradable, versatile structures (nanospheres or nanocapsules).	Controlled drug release, imaging, nanomedicine.

2.2. More on the LSPR effect

Plasmonics studies the nanoscale manipulation of optical signals at metal–dielectric interfaces. Inspired by photonics, it exploits unique properties of metallic nanostructures that enable routing and control of light at near-atomic scales [5]. The Localised Surface Plasmon Resonance (LSPR) effect occurs when conduction electrons in metallic nanoparticles collectively oscillate in resonance with incident electromagnetic radiation. Unlike propagating surface plasmons, which travel along metal–dielectric interfaces, LSPR is confined within the nanoparticle. This confinement produces highly localised electromagnetic fields near its surface.

The resonance condition depends on the nanoparticle's size, shape, and material, as well as the dielectric properties of its surrounding medium. At resonance, the interaction between light and the nanoparticle is strongly enhanced. This results in distinct absorption and scattering features that appear as vivid colours in colloidal suspensions of metal nanoparticles.

2.3. Applications to OSCs

2.3.1. Monometallic Nanoparticles

Early efforts to enhance organic solar cell performance with nanoparticles focused primarily on monometallic systems, especially Gold (Au) and Silver (Ag). Kaçuş *et al.* [6] reported that doping P3HT:PCBM active layers with 1 wt% of Au or Ag nanoparticles increased the power conversion efficiency from 2.11% (undoped) to 2.55% and 2.23%, respectively. These gains were attributed to improved optical absorption and surface roughness, without significant changes to the optical band gap. Li *et al.* [7] advanced this work by showing that Ag nanoparticle geometry plays a critical role: incorporating a combination of nanospheres and nanoprisms broadened light absorption via multiple resonance modes, resulting in a 17.91% increase in short-circuit current density and a 19.44% improvement in PCE. Similarly, Cao *et al.* [8] systematically compared nanocones, nanocuboids, nanocylinders, inverted cones,

nanospheres, and nanoprisms, concluding that nanoparticle shape strongly influences plasmonic behaviour and device efficiency.

2.3.2. Bimetallic Nanoparticles

The next step in nanoparticle engineering involved combining two metals to exploit their complementary properties. Ike *et al.* [9] incorporated Zn:Ni nanoparticles into the P3HT:PCBM active layer and observed an increase in PCE from 2.56% to 4.78%, while also highlighting the environmental advantages of Zn and Ni. Piralaee *et al.* [10] synthesised Au:Ag core-shell nanoparticles and achieved a 59% enhancement in short-circuit current, demonstrating the synergistic plasmonic effects of these noble metals. Mola *et al.* [11] extended the scope by probing Ag:Zn nanoparticles as interfacial layers in conventional OSC structures, showing their potential beyond active-layer doping. Geometry continued to be a critical parameter, as shown by Heidarzadeh *et al.* [12], who employed Al:Ag nanocylinders to improve light trapping and charge generation. Together, these studies emphasise that bimetallic nanoparticles can achieve superior performance enhancements compared to monometallic systems, particularly when material choice and morphology are carefully optimised.

2.3.3. Trimetallic Nanoparticles

More recent studies have explored trimetallic nanoparticles, which offer an even broader platform for tailoring optical and electronic properties. Mbuyise *et al.* [13] demonstrated that Au:Zn:Ni nanoparticles incorporated into P3HT:PCBM layers improved device efficiency by 54% at 4 wt% and 84% at 6 wt% loading. Similarly, Hamed *et al.* [14] synthesised Cu:Ni:Ag nanoparticles and reported efficiency enhancements of up to 85%. These findings indicate that introducing a third metal can generate synergistic effects beyond those achievable with bi-metallic systems. However, research on trimetallic nanoparticles in OSCs remains limited, with only a few reported studies and little systematic investigation of their mechanisms. This gap highlights the need for further exploration, providing the motivation for the present work.

2.4. References

[1] S. Horikoshi and N. Serpone, "Introduction to Nanoparticles," in *Microwaves in Nanoparticle Synthesis*, 2013, pp. 1–24.

[2] V. Balzani, "Nanoscience and nanotechnology: a personal view of a chemist," *small,* vol. 1, no. 3, pp. 278–283, 2005.

[3] S. Hasan, "A review on nanoparticles: their synthesis and types," *Res. J. Recent Sci,* vol. 2277, p. 2502, 2015.

[4] K. A. Altammar, "A review on nanoparticles: characteristics, synthesis, applications, and challenges," (in English), *Frontiers in Microbiology,* Review vol. Volume 14 - 2023, 2023–April–17 2023, doi: 10.3389/fmicb.2023.1155622.

[5] W. A. Murray and W. L. Barnes, "Plasmonic Materials," *Advanced Materials,* vol. 19, no. 22, pp. 3771–3782, 2007, doi: https://doi.org/10.1002/adma.200700678.

[6] H. Kaçuş, A. Baltakesmez, Z. Çaldıran, Ş. Aydoğan, M. Yılmaz, and M. Sevim, "Optical and electrical characterization of organic solar cells obtained using gold and silver metal nanoparticles," *Materials Today: Proceedings,* vol. 46, pp. 6986–6990, 2021/01/01/ 2021, doi: https://doi.org/10.1016/j.matpr.2021.03.276.

[7] X. Li, W. C. H. Choy, H. Lu, W. E. I. Sha, and A. H. P. Ho, "Efficiency Enhancement of Organic Solar Cells by Using Shape-Dependent Broadband Plasmonic Absorption in Metallic Nanoparticles," *Advanced Functional Materials,* vol. 23, no. 21, pp. 2728–2735, 2013, doi: https://doi.org/10.1002/adfm.201202476.

[8] L. Q. Cao, Z. He, W. E. I. Sha, and R. S. Chen, "Influence of Geometry of Metallic Nanoparticles on Absorption of Thin-Film Organic Solar Cells: A Critical Examination," *IEEE Access,* vol. 8, pp. 145950–145959, 2020, doi: 10.1109/ACCESS.2020.3014817.

[9] J. N. Ike, M. S. G. Hamed, and G. T. Mola, "Effective energy harvesting in thin film organic solar cells using Ni:Zn as bimetallic nanoparticles," *Journal of Physics and Chemistry of*

Solids, vol. 161, p. 110405, 2022/02/01/ 2022, doi: https://doi.org/10.1016/j.jpcs.2021.110405.

[10] M. Piralaee and A. Asgari, "Bimetallic core–shell nanoparticles to improve the absorption of P3HT: PCBM organic solar cell," *Appl. Opt.,* vol. 60, no. 29, pp. 9087–9094, 2021/10/10 2021, doi: 10.1364/AO.438140.

[11] G. T. Mola and E. A. A. Arbab, "Bimetallic nanocomposite as hole transport co-buffer layer in organic solar cell," *Applied Physics A,* vol. 123, no. 12, p. 772, 2017/11/15 2017, doi: 10.1007/s00339-017-1383-6.

[12] H. Heidarzadeh, A. Jangjoy, and H. Bahador, "Use of Coupled Al-Ag Bimetallic Cylindrical Nanoparticles to Improve the Photocurrent of a Thin-Film Silicon Solar Cell," *Plasmonics,* vol. 17, no. 3, pp. 1323–1329, 2022/06/01 2022, doi: 10.1007/s11468-022-01630-x.

[13] X. G. Mbuyise, E. A. Arbab, and G. T. Mola, "The effect of a trimetallic nanocomposite in the solar absorber layer of organic solar cells," *RSC advances,* vol. 9, no. 11, pp. 6070–6076, 2019.

[14] M. S. G. Hamed, A. Y A Ahmed, and G. T. Mola, "Suppressing charge recombination in disordered polymers blend medium," *Journal of Physics D: Applied Physics,* vol. 56, no. 40, p. 405101, 2023/07/06 2023, doi: 10.1088/1361-6463/ace1ff.

Chapter 3

Experimental method

3.1. Materials

All materials used in this study were sourced from Ossila.

3.2. Synthesis of Mn:Ni:Ce Nanocomposites

Mn:Ni:Ce nanocomposites (NCs) were successfully synthesised via a wet chemical processing method. Initially, 0.1 M $NiCl_2$ was prepared in 50 mL of deionised water, 0.1 M $MnCl_2$ in 40 mL of deionised water, and 0.1 M $Ce(NO_3)_3$ in 40 mL of deionised water. The nickel chloride solution was added dropwise to the manganese chloride solution under continuous stirring, followed by the gradational addition of the cerium nitrate solution to the mixed solution. Subsequently, a fourth solution of 0.1 M sodium hydroxide was added slowly dropwise into the above mixture while stirring. The resulting mixture was stirred on a magnetic stirrer at 40 °C for 3 h. The obtained product was filtered and washed several times with deionised water to remove impurities. Finally, the precipitate was dried under vacuum at 70 °C for 2 h, yielding the Mn:Ni:Ce nanocomposite spherical particles.

3.3. Active Layer Preparation

Solutions were prepared by dissolving 6 mg of [6,6]-phenyl-C_{61}-butyric acid methyl ester (PCBM) and 3 mg of poly[N-9′-heptadecanyl-2,7-carbazole-alt-5,5-(4′,7′-di-2-thienyl-2′,1′,3′-benzothiadiazole)] (PCDTBT) in 500 µL of chlorobenzene. Four separate solutions were prepared in opaque vials to minimise photodegradation, an issue which plagues light-absorbing materials [1]. To three of the solutions, Mn:Ni:Ce nanoparticles were added in amounts of 0.01, 0.02, and 0.03 mg, respectively, while one solution was kept pristine for reference. Magnetic stirring spheres were disinfected with chlorobenzene prior to use, and all waste solvent was collected for environmentally safe disposal. The solutions in containers

were sealed with parafilm material to prevent spillage and stirred at 50 °C and 800 rpm for 3 h.

3.4. Transparent Electrode Preparation

Conductive Indium Tin Oxide (ITO) substrates were first scrubbed with dish soap and cotton buds, followed by a sequential ultrasonic purification process. Substrates were immersed in deionised water, acetone, and isopropanol for 10 min each at approximately 18 °C in a bath filled with water, with the substrates placed in a beaker containing the respective solvent. The expended solvents were collected and disposed of in an environmentally responsible manner. Four cleaned substrates were prepared for device fabrication.

3.5. Device Fabrication

3.5.1. Spin coating

The conductive side of the ITO substrates was confirmed by multimeter testing, after which the substrates were annealed at 100 °C for 20 min. A 20 µL Zinc Oxide (ZnO) electron transport layer spin coated at 3500 rpm for 60 s and annealed at 100 °C for 10 minutes. The active layer solution was deposited at 1200 rpm for 40 s using 50 µL of the polymer:fullerene blend, followed by annealing once.

3.5.2. Electrode deposition

Top electrodes were deposited via vacuum thermal evaporation under a vacuum of 4–6 × 10^{-4} mbar. Layers comprised 14 nm of MoO_3 and 80 nm of Ag, deposited sequentially using separate tungsten crucibles. Devices were annealed post-deposition for 5 minutes.

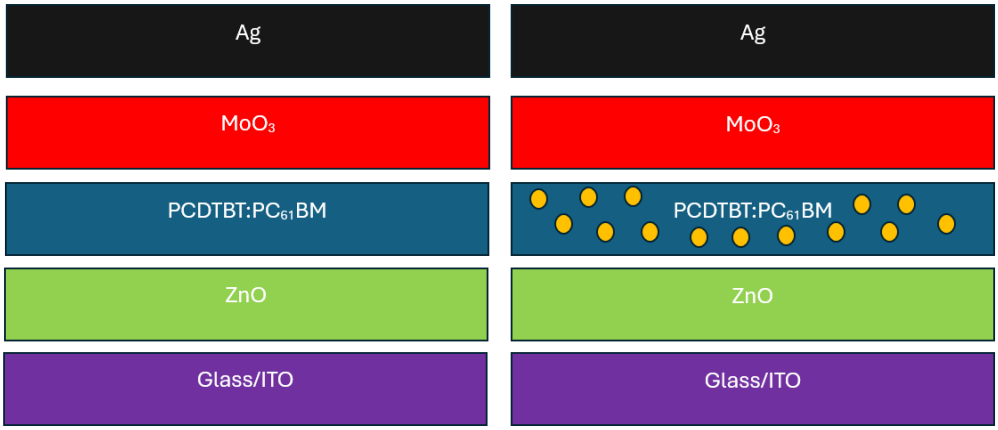

Figure 7: Schematic representation of a) Pristine b) Nanoparticle integrated BHJ photoactive layer in inverted organic solar cell architecture

3.6. Characterisation

3.6.1. Nanoparticle Characterisation

3.6.1.1. Energy Dispersive X-ray Spectroscopy

Energy Dispersive X-ray Spectroscopy (EDS) is a methodology used to identify the elemental composition of a material by analysing its characteristic X-ray spectrum. In this process, the primary electron beam dislodges an electron from an inner orbital shell of a sample atom, creating an unstable, excited state. When an electron from a higher energy shell fills this vacancy, the energy difference between the shells is released as an X-ray photon with a characteristic energy unique to the element. This characteristic energy facilitates the identification of the elements present within the sample [2]. Consequently, EDS analysis was performed using Backscattered Electrons (BSE), with elemental mapping conducted via Aztec software for spatial visualisation.

3.6.1.2. Scanning Electron Microscopy

Scanning Electron Microscopy (SEM) is a technique that magnifies samples by directing a focused beam of electrons onto their surfaces. The electron beam is typically generated either through thermionic emission from a filament, often made of tungsten (W), or by field emission from a sharp tip. Within a high-vacuum chamber, this beam is precisely controlled, condensed, and focused onto the sample using a sequence of electromagnetic lenses and apertures; the

specific designs of these components may vary depending on the microscope manufacturer [3]. In this study, imaging of the nanoparticles was performed using a Zeiss Crossbeam 540 SEM system with the instrument maintained at an Electron High Tension (EHT) of 2.00 kV and a Working Distance (WD) of 2.5 mm under high vacuum.

Figure 8: Zeiss Crossbeam 540 used in SEM and EDS analysis

3.6.2. Device Electrical Characterisation

3.6.2.1. Power Conversion Efficiency

The Power conversion efficiency (PCE), occasionally denoted by η, represents the percentage of input irradiation that is converted into output power by a photovoltaic device, calculated as the product of open-circuit voltage, short-circuit current, and fill factor divided by the input power.

$$\mathrm{PCE} = \frac{J_{SC} \times V_{OC} \times FF}{P_{IN}} \times 100$$

Where:

- J_{SC} is short circuit current
- V_{OC} is Open circuit voltage
- FF is Fill Factor
- P_{IN} is the Power input

The PCE is determined from measurements of current density-voltage (J-V) characteristics of the device. In this study, the J-V characteristics values were measured automatically using an Ossila Solar Simulator (figure) measurement system. The illumination conditions were set to standard testing parameters: 1 Sun (1000 W/m^2) intensity, AM1.5 spectral distribution, and room temperature. Both dark and light current measurements were performed: under illumination from −1 V to 1 V, in the dark for the same range, and additionally from -3 V to 3 V to capture the full current–voltage response.

Figure 9: Ossila Solar Simulator used for PCE measurements

3.6.2.2. Quantum Efficiency

Quantum Efficiency (QE) is defined as the ratio of the total number of charge carriers collected by the solar cell to the number of photons of a given energy that shine on and are absorbed by the cell from outside [4]. By studying the solar spectrum for each solar cell, ways to broaden the spectrum region to maximise the use of the spectrum could be found. QE is influenced by several factors including the electron-hole charge balance facet, the fraction of excitons decaying via radiative pathways, and the intrinsic quantum efficiency for radiative decay [5].

A low QE indicates poor utilisation of absorbed photons by the photoactive layer, often due to poor carrier collection efficiency. This inefficiency directly impacts PCE, making QE a crucial parameter in evaluating solar cell performance, which is highly relevant to this paper. A quantity closely related to QE is Spectral Response (SR) which describes how efficiently the solar cell converts light of different wavelengths into electrical current. [6].

$$SR(\lambda) = \frac{I_{PH}(\lambda)}{P_{IN}(\lambda)}$$

Where:

- I_{PH} is incident current
- P_{IN} is input power
- λ is the wavelength

Mathematically, the relationship between SR and QE is:

$$QE = \frac{SR(\lambda) \times h \times c}{e \times \lambda}$$

Where:

- h is planks constant
- c is the speed of light in a vacuum
- e is the charge of an electron

In this investigation, QE and SR measurements were performed after calibrating the instrument with a silicon reference cell, which served as a standard to ensure measurement accuracy and reliability.

Figure 10: Part of the Oriel Newport QE-PV-SI system used for calculating quantum efficiency

3.6.3. Spectroscopy

3.6.3.1. Ultraviolet and Visible Spectroscopy

Ultraviolet and Visible spectroscopy (UV-Vis) is an optical spectroscopy technique that utilises light in the ultraviolet, visible, and near-infrared ranges. It is based on the Beer-Lambert law, which states that the absorbance of a solution is directly proportional to the concentration of the absorbing species and the path length of the light through the sample [7, 8]. UV-Vis absorption measures the intensity of light transmitted through a sample compared to the initial light intensity. The typical scan range for UV-Vis absorption spans from 200 to 400 nm for ultraviolet light and from 400 to 800 nm for visible light. Prior to the assessment of the solar devices, baseline correction was performed using deionised water and clean ITO substrates, with the coated side facing the light source to ensure accurate absorbance measurements.

Figure 11: Agilent Cary 60 Uv-Vis Apparatus

3.6.3.2. Impedance Spectroscopy

The impedance of a conductor is its apparent resistance expressed in ohms [9]. Impedance spectroscopy (IS) is a blanket term that encompasses the small signal measurement of the linear electrical response of a material of interest and the sequential analysis of the response to produce useful information about the physicochemical properties of the system [10]. Using methodology comprehensively discussed by Yadav et al. [11], impedance spectra of the samples are taken recorded an Ossila Four Point Probe (figure 12) from the range 20 Hz to 20 MHz at toom temperature.

Figure 12: Ossila Four Point Probe system

3.7. References

[1] E. Yousif and R. Haddad, "Photodegradation and photostabilization of polymers, especially polystyrene: review," (in eng), *Springerplus,* vol. 2, p. 398, 2013, doi: 10.1186/2193-1801-2-398.

[2] D. E. Newbury and N. W. M. Ritchie, "Performing elemental microanalysis with high accuracy and high precision by scanning electron microscopy/silicon drift detector energy-dispersive X-ray spectrometry (SEM/SDD-EDS)," *Journal of Materials Science,* vol. 50, no. 2, pp. 493–518, 2015/01/01 2015, doi: 10.1007/s10853-014-8685-2.

[3] A. Mohammed and A. Abdullah, "Scanning electron microscopy (SEM): A review," in *Proceedings of the 2018 international conference on hydraulics and pneumatics—HERVEX, Băile Govora, Romania*, 2018, vol. 2018, pp. 7–9.

[4] W. J. Yang, Z. Q. Ma, X. Tang, C. B. Feng, W. G. Zhao, and P. P. Shi, "Internal quantum efficiency for solar cells," *Solar Energy,* vol. 82, no. 2, pp. 106–110, 2008/02/01/ 2008, doi: https://doi.org/10.1016/j.solener.2007.07.010.

[5] F. Wang, X.-K. Liu, and F. Gao, "Chapter 1 - Fundamentals of Solar Cells and Light-Emitting Diodes," in *Advanced Nanomaterials for Solar Cells and Light Emitting Diodes*, F. Gao Ed.: Elsevier, 2019, pp. 1–35.

[6] J. S. Hartman and M. A. Lind, "Spectral response measurements for solar cells," *Solar Cells,* vol. 7, no. 1, pp. 147–157, 1982/11/01/ 1982, doi: https://doi.org/10.1016/0379-6787(82)90099-0.

[7] H. Förster, "UV/vis spectroscopy," in *Characterization I: -/-*: Springer, 2004, pp. 337–426.

[8] A. Klamt, "Calculation of UV/Vis spectra in solution," *The Journal of Physical Chemistry,* vol. 100, no. 9, pp. 3349–3353, 1996.

[9] A. E. Kennelly, "Impedance," *Transactions of the American Institute of Electrical Engineers,* vol. 10, pp. 172–232, 1893.

[10] J. R. Macdonald, "Impedance spectroscopy," *Annals of Biomedical Engineering,* vol. 20, no. 3, pp. 289–305, 1992/05/01 1992, doi: 10.1007/BF02368532.

[11] P. Yadav, K. Pandey, V. Bhatt, M. Kumar, and J. Kim, "Critical aspects of impedance spectroscopy in silicon solar cell characterization: A review," *Renewable and Sustainable Energy Reviews,* vol. 76, pp. 1562–1578, 2017/09/01/ 2017, doi: https://doi.org/10.1016/j.rser.2016.11.205.

Chapter 4

Results and discussion

4.1. Introduction

In this chapter, the morphology of the synthesised nanoparticle composites prepared via a wet chemical process is presented and analysed. Furthermore, the electrical characteristics of the fabricated solar cells are discussed in detail and compared with relevant findings from the literature to evaluate their performance and consistency with reported studies.

4.2. Properties of Nanoparticles

4.2.1. Morphology and structure nanoparticles.

SEM analysis revealed that the nanoparticles are predominantly spherical in shape, which is one of the most readily achievable morphologies in laboratory synthesis [1, 2]. The spherical structures exhibit an average diameter of approximately 62 nm. However, their distribution across the crystal surface is relatively non-uniform. The surface frequently displays straight, smooth planes interspersed with these spherical features, suggesting a structural tendency toward planar growth accompanied by localised spherical formations.

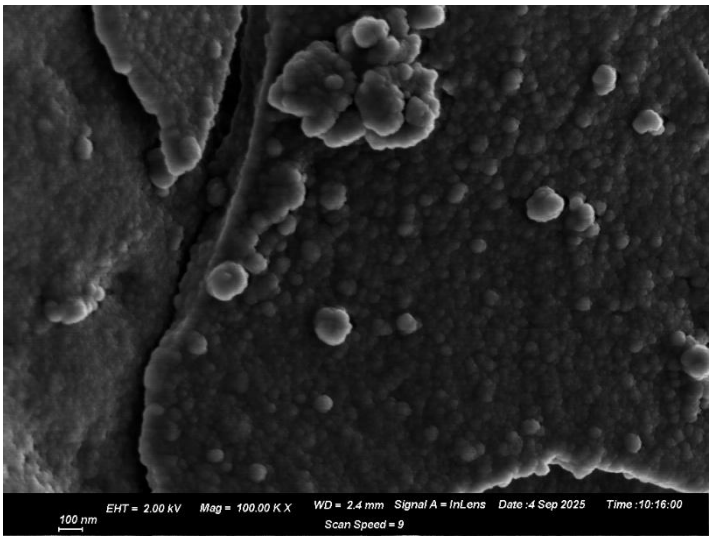

Figure 13: SEM image showing structure and shape of Mn:Ni:Ce trimetallic nanocomposite

EDS elemental mapping indicates that the synthesised nanoparticles are highly dominated by cerium (Ce), accounting for approximately 99.3 wt%. This result suggests that the synthesis process did not yield the intended trimetallic nanoparticle nanocomposite [3]. Instead, it primarily produced nearly pure cerium particles, with negligible incorporation of the other intended metallic elements. This outcome is generally unfavourable, as the absence of the other two metallic components likely limits the enhancement of the LSPR phenomenon.

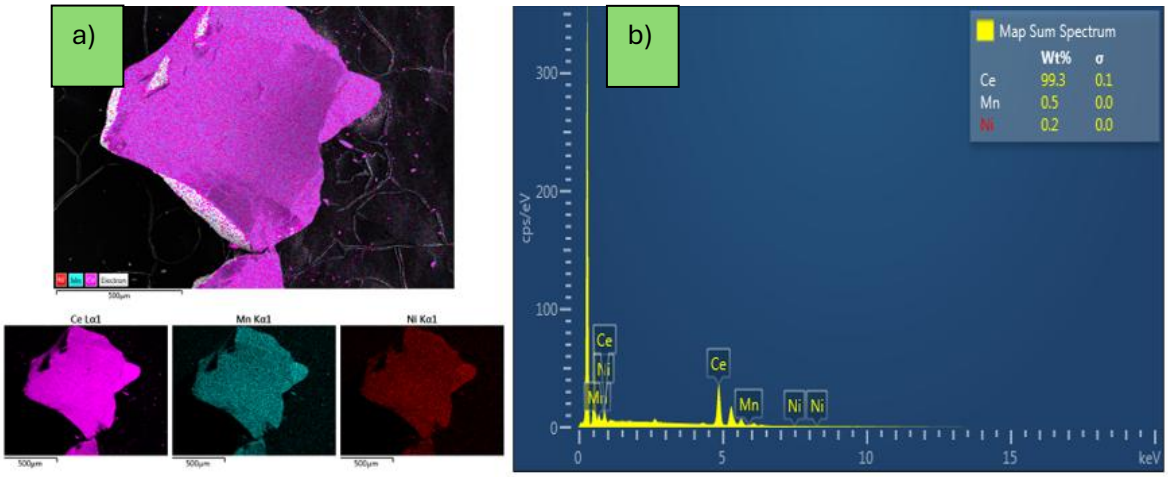

Figure 14: a) EDS Elemental Map and b) %wt composition of Mn:Ni:Ce nanocomposite

4.3. Electrical Properties of Organic Solar Cell

4.3.1. J-V characteristics

Analysis of the J–V characteristics shows that the solar cell with the highest power conversion efficiency (PCE) of 6.63% is the NP1% sample. This efficiency is approximately three times greater than that of the pristine cell, which has a PCE of 2.16%. Both the NP2% and NP3% samples exhibit about a 1% increase in PCE compared to the pristine cell. However, these results indicate diminishing returns when nanoparticle concentration increases beyond 1%.

Among all devices tested, adding 1% nanoparticles leads to a 10% increase in the fill factor (FF) and significant improvements in the short-circuit current density (J_{SC}) and open-circuit voltage (V_{OC}). These parameters, shown as intercepts in the J–V plots in figure 15 (a-d), directly impact the overall efficiency.

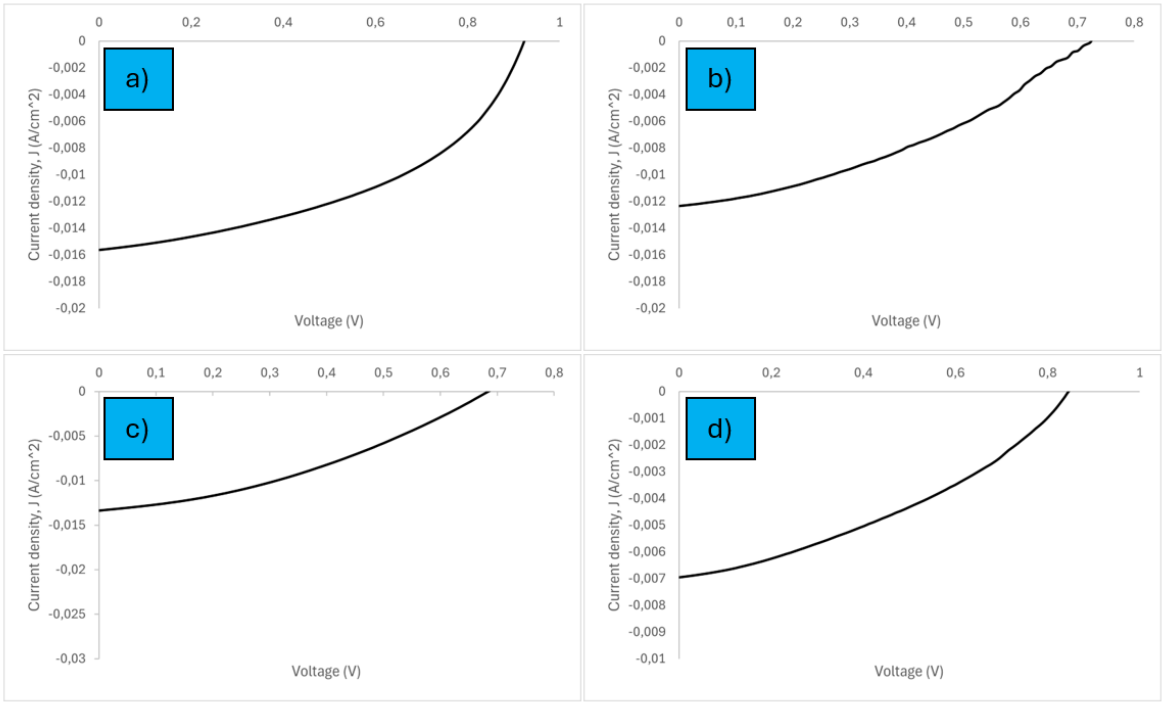

Figure 15: J-V characteristic of a) Pristine, b) 1% Nanoparticles, c) 2% Nanoparticles, and d) 3% Nanoparticles incorporated solar cell devices

The pristine sample shows the highest shunt resistance, which decreases progressively with higher nanoparticle concentrations. However, shunt resistance changes alone do not fully explain the performance variations. Notably, the NP1% device has the lowest series resistance, which further contributes to its superior performance.

At higher nanoparticle loadings, the performance declines likely due to nanoparticle aggregation [4]. Aggregates increase charge recombination and reduce uniform light absorption, which limits efficiency gains.

This trend suggests that moderate nanoparticle incorporation improves charge transport and light absorption through LSPR effects. In contrast, excessive nanoparticle loading disrupts film morphology and charge pathways, as discussed by Wang et al [5].

At the optimal 1% nanoparticle concentration, the nanoparticles are well-distributed, enabling efficient coupling between plasmonic fields and the semiconductor matrix. This uniform distribution enhances charge separation and minimises recombination losses, as seen in the

increased J_{SC} and V_{OC} [6]. Moreover, the lower series resistance in the NP1% cell indicates improved charge transport, helping to raise the fill factor.

Beyond this optimal point, particle aggregation dominates, acting as recombination centres and scattering light non-productively. These effects degrade both optical and electrical performance, explaining the diminishing returns in PCE for the NP2% and NP3% samples.

Table 2: Summary of performance analytics of fabricated organic solar cell devices

Cell	PCE (%)	FF (%)	Jsc (A.cm^-2)	Voc (V)	Maximum Power (W)	Vmp (V)	Jmp (A.cm^-2)	R Shunt (Ohm. cm^2)	R Series (Ohm. cm^2)
Pristine	2,1670	36,8958	-0,0069	0,8454	0,0022	0,5301	-0,0041	457,6751	38,3299
NP1%	6,6261	45,8780	-0,0156	0,9234	0,0066	0,6500	-0,0102	263,3794	11,3056
NP2%	3,2317	36,1504	-0,0123	0,7240	0,0032	0,4414	-0,0073	216,0823	27,4183
NP3%	3,2943	36,0161	-0,0134	0,6843	0,0033	0,3923	-0,0084	161,3946	27,6459

4.3.2. Quantum efficiency

The pristine device exhibits measurable quantum efficiency QE within the spectral range of 310–830 nm, with a peak of approximately 48% at 390 nm in the near-UV/blue region. Beyond this range, the EQE becomes negligible, indicating minimal photoresponse for longer wavelengths.

Incorporation of nanoparticles significantly alters the spectral response. The NP1% device extends the measurable QE range from the near-UV (~300 nm) into the near-infrared (beyond 800 nm), with a peak efficiency similar in magnitude (~48%) but shifted toward longer wavelengths around 560 nm. This redshift suggests that the nanoparticles enhance light absorption and charge conversion over a broader spectral range LSPR effects that increase optical field confinement and scattering within the active layer.

The NP2% device demonstrates the highest peak EQE (~59%) at 390 nm, maintaining strong photoresponse from 310 nm to 800 nm. The higher peak and blue shifted maximum relative to NP1% indicate that moderate increases in nanoparticle concentration further improve

photon harvesting in the near-UV/blue region, possibly due to enhanced plasmonic coupling and more efficient light–matter interactions.

The NP3% device retains a broad photoresponse over 310–800 nm, with a peak of approximately 43% at 550 nm. While the spectral shape resembles that of NP1% and NP2%, the reduced peak intensity suggests that excessive nanoparticle loading leads to aggregation and increased carrier recombination, thereby diminishing charge collection efficiency.

Overall, the QE analysis confirms that nanoparticle incorporation extends the device's spectral sensitivity and enhances photoresponse, but optimal performance occurs at moderate loading (1–2%), where plasmonic enhancement and film uniformity are best balanced.

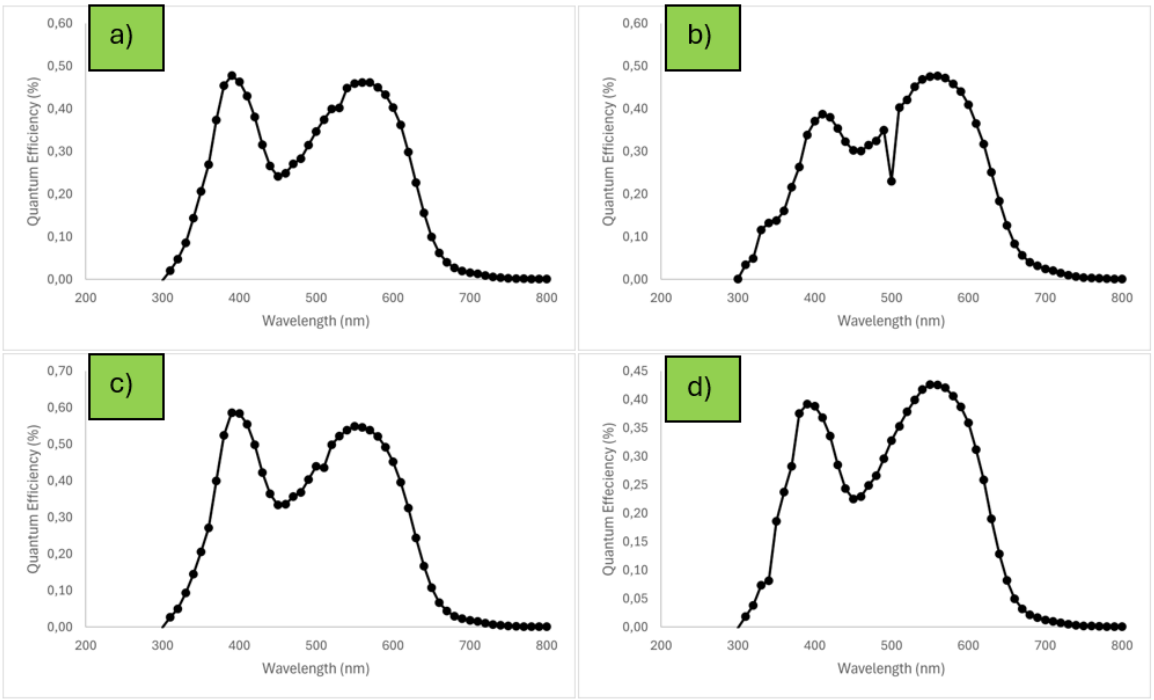

Figure 16: Quantum efficiencies of a) Pristine, b) 1% Nanoparticles, c) 2% Nanoparticles, and d) 3% Nanoparticles incorporated organic solar cell devices

4.3.3. UV-Vis

Analysis of the UV–Vis absorption spectra reveals that the integration of nanoparticles does not drastically alter the overall absorption behaviour; instead, all samples exhibit a similar trend. The devices display strong absorption in both the ultraviolet (UV) and visible regions, with absorbance values ranging between 0.5 and 0.8 near 800 nm. The spectra generally

diminish toward shorter wavelengths, indicating efficient absorption in the UV–visible range followed by a gradual decline into the infrared (IR) region.

The pristine cell exhibits a peak absorbance of 0.582 at 860 nm. Upon nanoparticle incorporation, noticeable variations in peak intensity and wavelength position are observed. The NC1% sample shows the highest peak absorbance of 0.87 at 820 nm, followed by NC2% with a peak of 0.69 at 820 nm, and NC3% with 0.61 at 900 nm.

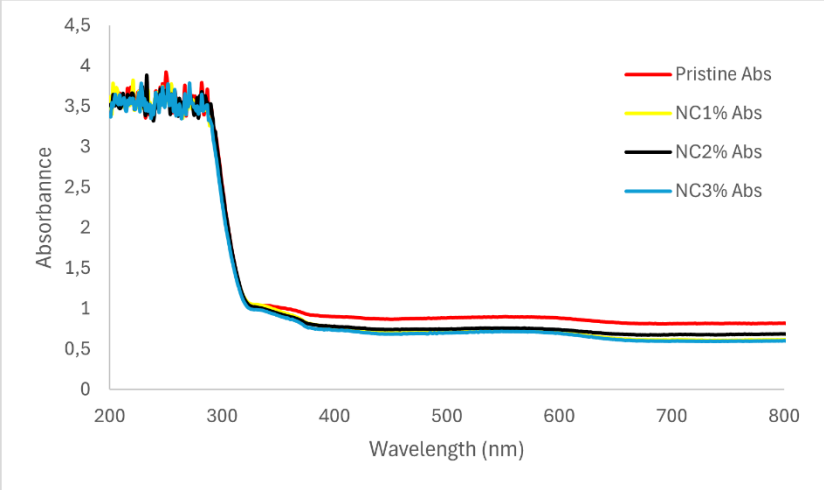

4.3.4. Impedance

The Nyquist plots in Figure 17 (a–d) represent the impedance characteristics of the pristine, NP1%, NP2%, and NP3% devices, respectively. Each semicircular arc corresponds to the charge-transfer resistance (R_{CT}), which is inversely related to the efficiency of charge transport through the device. A smaller arc indicates lower resistance and improved charge mobility, while a larger arc signifies higher resistance and hindered carrier transport [7, 8].

The pristine device (Figure 17 a) shows a moderate semicircular arc, reflecting balanced charge transport and relatively low recombination losses. Upon the incorporation of 1% nanoparticles (Figure 17 b), the arc diameter increases slightly, indicating a rise in charge-transfer resistance. However, the arc shape remains uniform and well defined, suggesting consistent charge transport behaviour across different frequencies. Despite the moderate increase in R_{CT}, NP1% maintains the most stable and uniform impedance response, consistent with its superior photovoltaic performance and highest PCE of 6.63%.

The NP2% device (Figure 17 c) displays a smaller semicircular arc than NP1%, suggesting lower average resistance. Nonetheless, the arcs are unevenly spaced and irregular across frequencies, implying that charge transport is less uniform and potentially unstable. This non-uniformity may result in localised recombination and explains the diminishing performance gains beyond 1% nanoparticle loading.

In contrast, the NP3% device (Figure 17 d) exhibits a significantly larger and highly distorted semicircular arc, indicative of substantial charge-transfer resistance and poor carrier mobility. The pronounced separation between arcs at different voltages reveals non-uniform charge transport and severe recombination losses.

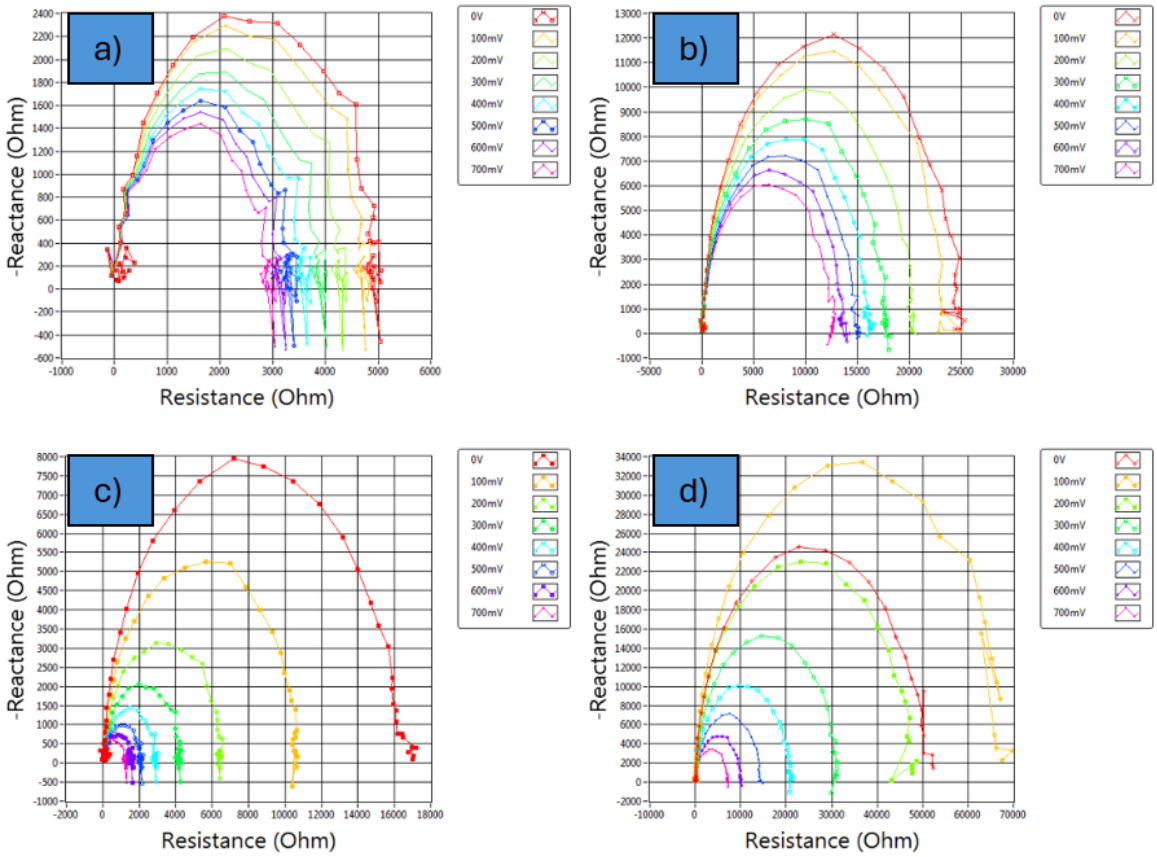

Figure 17: Nyquist plot of a) Pristine, b) 1% Nanoparticles, c) 2% Nanoparticles, and d) 3% Nanoparticles incorporated organic solar cell devices

4.4. Conclusion

In this study, optimal nanoparticle incorporation (~1%) was found to significantly enhance the performance of the fabricated solar cells. Morphological and optical analyses revealed that

nanoparticle addition improved light absorption and extended spectral response into the near-infrared region. The NP1% device achieved the highest power conversion efficiency (6.63%), supported by improved fill factor, current density, and voltage. Although NP2% exhibited slightly lower resistance, impedance analysis showed that NP1% maintained more uniform and stable charge transport. Excessive nanoparticle loading (≥3%) led to aggregation and recombination losses, confirming that controlled nanoparticle concentration is key to balancing optical enhancement and efficient charge transport for optimal solar cell performance

4.5. References

[1] K. A. Altammar, "A review on nanoparticles: characteristics, synthesis, applications, and challenges," (in English), *Frontiers in Microbiology,* Review vol. Volume 14 - 2023, 2023–April–17 2023, doi: 10.3389/fmicb.2023.1155622.

[2] S. Hasan, "A review on nanoparticles: their synthesis and types," *Res. J. Recent Sci,* vol. 2277, p. 2502, 2015.

[3] R. Ferrando, J. Jellinek, and R. L. Johnston, "Nanoalloys: From Theory to Applications of Alloy Clusters and Nanoparticles," *Chemical Reviews,* vol. 108, no. 3, pp. 845–910, 2008/03/01 2008, doi: 10.1021/cr040090g.

[4] P. Li *et al.*, "Solvents Induced ZnO Nanoparticles Aggregation Associated with Their Interfacial Effect on Organic Solar Cells," *ACS Applied Materials & Interfaces,* vol. 6, no. 20, pp. 18172–18179, 2014/10/22 2014, doi: 10.1021/am5051789.

[5] L. Wang, J. Luo, M. J. Schadt, and C.-J. Zhong, "Thin Film Assemblies of Molecularly-Linked Metal Nanoparticles and Multifunctional Properties," *Langmuir,* vol. 26, no. 2, pp. 618–632, 2010/01/19 2010, doi: 10.1021/la901811g.

[6] O. J. Sandberg, A. Sundqvist, M. Nyman, and R. Österbacka, "Relating Charge Transport, Contact Properties, and Recombination to Open-Circuit Voltage in Sandwich-Type Thin-Film Solar Cells," *Physical Review Applied,* vol. 5, no. 4, p. 044005, 04/12/ 2016, doi: 10.1103/PhysRevApplied.5.044005.

[7] F. Fabregat-Santiago, G. a. Garcia-Belmonte, I. a. Mora-Serâo, and J. Bisquert, "Characterization of nanostructured hybrid and organic solar cells by impedance spectroscopy," *Physical Chemistry Chemical Physics (Incorporating Faraday Transactions),* vol. 13, no. 20, pp. 9083–9118, 2011, doi: 10.1039/c0cp02249g.

[8] E. von Hauff, "Impedance Spectroscopy for Emerging Photovoltaics," *The Journal of Physical Chemistry C,* vol. 123, no. 18, pp. 11329–11346, 2019, doi: 10.1021/acs.jpcc.9b00892.

Chapter 5

Conclusion

5.1. Closing remarks

Comprehensive characterisation of the nanoparticle-modified solar cells demonstrated that nanoparticle concentration has a pronounced influence on the optical and electrical performance of the devices. Morphological analysis revealed that the synthesised nanoparticles were predominantly spherical with an average diameter of around 62 nm. However, EDS results indicated a strong cerium dominance, suggesting incomplete formation of the intended trimetallic nanocomposite.

Optical characterisation through UV–Vis spectroscopy showed strong absorption in the UV–visible range with a gradual decline into the infrared region. Incorporation of nanoparticles caused subtle shifts and intensity variations in the absorption peaks, particularly in the near-infrared, signifying enhanced light–matter interaction due to nanostructuring. The QE analysis further confirmed this improvement, revealing extended photoresponse up to 800 nm and higher quantum efficiency in the NP1% and NP2% devices, consistent with better photon harvesting and charge generation.

Electrical characterisation through J–V measurements identified the NP1% device as the best-performing cell, achieving a PCE of 6.63%, nearly triple that of the pristine sample. This improvement stemmed from higher fill factor, short-circuit current density, and open-circuit voltage, alongside reduced series resistance. Impedance analysis supported these findings: although NP2% exhibited slightly lower resistance, NP1% demonstrated more uniform and stable charge transport across frequencies, while NP3% suffered from high resistance and severe non-uniformity.

5.2. Future Work

Due to the scope and constraints of this research project, several characterisation techniques could not be performed. Future studies should include advanced structural and compositional analyses such as X-ray diffraction (XRD), Raman spectroscopy, and transmission electron microscopy (TEM) to gain deeper insight into the crystallinity, phase composition, and particle distribution within the nanocomposite. Additionally, conducting EDS and SEM analyses on the fully fabricated solar cell devices would provide valuable information on the uniformity, morphology, and elemental integration of the nanoparticles within the BHJ layer. These additional measurements would help establish a more comprehensive understanding of how nanocomposite incorporation influences device structure and overall photovoltaic performance.